

# InstantSplat: Sparse-view SfM-free Gaussian Splatting in Seconds

Zhiwen Fan<sup>\*†1,2</sup>, Wenyan Cong<sup>\*1</sup>, Kairun Wen<sup>\*3</sup>, Kevin Wang<sup>1</sup>, Jian Zhang<sup>3</sup>, Xinghao Ding<sup>3</sup>, Danfei Xu<sup>2,4</sup>, Boris Ivanovic<sup>2</sup>, Marco Pavone<sup>2,5</sup>, Georgios Pavlakos<sup>1</sup>, Zhangyang Wang<sup>1</sup>, Yue Wang<sup>2,6</sup>

\* Equal contribution † Project leader

<sup>1</sup>University of Texas at Austin <sup>2</sup>Nvidia Research <sup>3</sup>Xiamen University

<sup>4</sup>Georgia Institute of Technology <sup>5</sup>Stanford University <sup>6</sup>University of Southern California



Figure 1. **Novel View Synthesis Comparisons (Sparse-View w/o Structure-from-Motion Preprocessing).** We introduce InstantSplat, an efficient framework for novel view synthesis from sparse-view unposed inputs. This approach incorporates densely geometric priors derived from multi-view stereo, a gradient-based joint optimization framework capable of reconstructing 3D scenes and synthesizing novel views in seconds, for large-scale scenes. Moreover, our method remarkably enhances both pose estimation accuracy and rendering quality than previous unposed methods.

## Abstract

While novel view synthesis (NVS) from a sparse set of images has advanced significantly in 3D computer vision, it relies on precise initial estimation of camera parameters using Structure-from-Motion (SfM). For instance, the recently developed Gaussian Splatting depends heavily on the accuracy of SfM-derived points and poses. However, SfM processes are time-consuming and often prove unreliable in sparse-view scenarios, where matched features are scarce, leading to accumulated errors and limited generalization capability across datasets. In this study, we introduce a novel and efficient framework to enhance robust NVS from sparse-view images. Our framework, **InstantSplat**, integrates multi-view stereo(MVS) predictions with point-based representations to construct 3D Gaussians of large-scale scenes from sparse-view data within seconds, addressing the aforementioned performance and efficiency issues by SfM. Specifically, InstantSplat generates densely populated surface points across all training views and determines the initial camera parameters using pixel-alignment. Nonetheless, the MVS points are not globally accurate, and the pixel-wise prediction from all views results in an excessive Gaussian number, yielding a over-parameterized scene representation that compromises both

training speed and accuracy. To address this issue, we employ a grid-based, confidence-aware Farthest Point Sampling to strategically position point primitives at representative locations in parallel. Next, we enhance pose accuracy and tune scene parameters through a gradient-based joint optimization framework from self-supervision. By employing this simplified framework, InstantSplat achieves a substantial reduction in training time—from hours to mere seconds—and demonstrates robust performance across various numbers of views in diverse datasets. Project page: <https://instantsplat.github.io/>.

## 1. Introduction

Novel-view synthesis (NVS) has been a long-standing goal in computer vision. It involves rendering images at arbitrary viewpoints that are unseen during training. However, capturing scenes in a “casual” manner, with a limited number of observed views (referred to as sparse-view) using low-cost sensors (such as smartphones), is even more challenging. Therefore, adopting an efficient framework that reconstructs 3D scenes directly from few uncalibrated images is essential for scaling up 3D content creation, digital twin construction, energy-efficient robots, and augmented reality applications.

Despite recent advancements [13, 24, 32, 40] that have

shown notable progress in reducing the required number of training views, a significant challenge in sparse-view synthesis (SVS) remains unresolved: The sparse input data often lack sufficient overlap, preventing Structure from Motion (SfM) pipelines like COLMAP [27] from estimating accurate camera parameters. Previous research in SVS [13, 24] typically assumes precise camera poses even in sparse-view scenarios by leveraging dense views for pre-computation, an assumption that is rarely valid. Moreover, the accumulated errors from the SfM step may propagate to subsequent steps, leading to suboptimal reconstruction and view synthesis. Another line of research explores pose-free settings in NeRFmm [35], Nope-NeRF [5] and CF-3DGS [10]. They also assume dense data coverage, often sourced from video sequences. Such dense data requires an extensive optimization process, usually requires hours for a single 3D scene.

More recently, 3D Gaussian Splatting (3D-GS)[16] has been introduced as an expressive and efficient scene representation technique, facilitating both high-speed and high-fidelity training and rendering. This method utilizes an optimized set of anisotropic 3D Gaussians, initialized at points derived from COLMAP. The optimization process is driven by a multi-view photometric loss and is complemented by Adaptive Density Control (ADC), a heuristic that governs the creation or deletion of 3D primitives. However, due to the varying number of points created by COLMAP, ADC parameters are tuned for each scene and significantly affect the performance of 3D-GS. As illustrated in Tab. 1, merely lowering the densification threshold to promote the generation of more primitives markedly enhances the reconstruction quality in the “Scene Bicycle”. Therefore, 3D-GS also suffers from view sparsity and the dependence of COLMAP, despite achieving state-of-the-art view synthesis performance.

In this paper, we present **InstantSplat**, to deliver an efficient and reliable framework for processing sparse-view data. We investigate the limitations in 3D-GS and identify key issues including the SfM preprocessing and the complex ADC [16] as mentioned above. To that end, InstantSplat integrates explicit 3D-GS with geometric priors from learning-based MVS [11, 41]. First, it leverages DUS3R [33] to generate a set of densely covered and pixel-aligned points, capturing adequate scene geometry for 3D-GS primitive initialization. However, these over-parameterized primitives hinder both the performance and speed of 3D-GS optimization. To address this issue, we introduce a parallel grid partitioning strategy with a farthest point sampling as a downsample to only retain the Gaussians with high confidence. Second, we jointly optimize Gaussian attributes and camera parameters, to refine scene representation and camera trajectory simultaneously. This allows us to correct the accumulated errors from

	SSIM $\uparrow$	LPIPS $\downarrow$
COLMAP+3DGS [16]	0.7633	0.2122
+ Adjust ADC Threshd.	0.7817 <sub>(+0.0184)</sub>	0.1666 <sub>(-0.0456)</sub>
+ Mask 30% SfM Points	0.7406 <sub>(-0.0227)</sub>	0.2427 <sub>(+0.0305)</sub>
$\pm 5^\circ$ Noise on Rotation	0.2999 <sub>(-0.4634)</sub>	0.5879 <sub>(+0.3757)</sub>

Table 1. **Sensitivity Analysis in Adaptive Density Control (ADC).** 3D-GS [16] proposes an optimization strategy where Gaussians were initialized from the Structure-from-Motion (SfM) point cloud and poses. However, simple adjusting a the densification gradient threshold (a ADC parameter [16]) to half can significantly enhance rendering quality (LPIPS: 0.2122  $\mapsto$  0.1666). Non-uniformly distributed points (30%), introduced by downsampling, present significant challenges for 3D-GS optimization (LPIPS: 0.2122  $\mapsto$  0.2427). The optimization is notably sensitive to noise in the camera pose, with even slight rotational perturbations causing issues (LPIPS: 0.2122  $\mapsto$  0.5879). This motivates us to design a more robust and general pipeline for 3D modeling. Experiments are on “Bicycle” scene from MipNeRF360 datasets.

the MVS step and produce a precise representation of the scene without the need for ADC. Our experiments, conducted on datasets including MVIImgNet [43], Tanks and Temples [17], MipNeRF360 [2], and in-the-wild Internet data, suggest that our method not only reduces the optimization time from 33 minutes (NoPe-NeRF) to merely 10.4 seconds (Ours-S), but also achieves a 62% improvement in SSIM and significant enhancements in pose metrics.

## 2. Related Works

**3D Representations for NVS** Novel view synthesis aims to generate unseen views of an object or scene from a given set of images [1, 22]. Neural Radiance Fields (NeRF)[23], enables photo-realistic rendering quality, employs MLPs to represent 3D scenes, taking the directions and positions of 3D points as input and employing volume rendering for image synthesis. Despite its popularity, NeRF faces challenges in terms of speed during both training and inference phases. Subsequent enhancements primarily focus on either enhancing quality[2–4] or improving efficiency [25, 28–30], with few achieving both. Recent advancements in unstructured radiance fields[6, 16, 39] introduce a set of primitives to represent scenes. Notably, 3D Gaussian Splatting (3D-GS) [16] uses anisotropic 3D Gaussians [46] to depict radiance fields, coupled with differentiable splatting for rendering. This method has shown considerable success in rapidly reconstructing complex real-world scenes with high quality. However, 3D-GS involves a large number of hyper-parameters for different datasets, especially for the adaptive density control, which servers as the core function to densify from sparse SfM point cloud to densely covered 3D Gaussian points. However, the optimization of SfM is independent with the followed 3D Gaussian optimization, and the accumulated error cannot be mitigated with current pipelines. This motivate us to design a holistic, efficient and

robust framework to represent the 3D world.

**Unconstraint Novel View Synthesis** NeRFs and 3DGS require carefully captured hundreds of images to ensure sufficient scene coverage as input and utilize pre-processing Structure-from-Motion (SfM) software, such as COLMAP [27], to compute camera parameters, and sparse SfM point cloud as additional inputs. However, the densely captured images with the strong reliance on COLMAP significantly limits practical applications, it requires the users with expertise in the field of photography and requires significant computing resources (hours for each individual scene). The accumulated error from SfM will propagate to the following differential 3D representation and SfM may fail with captured images without sufficient overlappings and rich textures. To address the challenge of the requisite number of views, various studies have introduced different regularization techniques to optimize the radiance fields. For instance, Depth-NeRF [8] employs additional depth supervision to enhance rendering quality. RegNeRF [24] and SparseNeRF [32] introduces a depth prior loss for geometric regularization. DietNeRF [13], SinNeRF [38], and ReconFusion [36] leverages supervision in the CLIP/DINO-ViT/Diffusion Model to constrain the rendering of unseen views. PixelNeRF [42] and FreeNeRF [40] utilize pre-training and frequency annealing for few-shot NeRF. FSGS [45], and SparseGS [37] employ monocular depth estimators or diffusion models on Gaussian Splatting for sparse-view conditions. However, these methods require known ground-truth camera poses computed and sampled from using dense views in the preprocessing, and Structure-from-Motion (SfM) algorithms often fail to predict camera poses and point cloud with sparse inputs due to insufficient image correspondences. Therefore, another line of research focuses on pose-free 3D optimization with uncalibrated images as direct input. NeRFm [35] simultaneously optimizes camera intrinsics, extrinsics, and NeRF training. BARF [19] introduces a coarse-to-fine strategy for encoding camera poses and joint NeRF optimization. SCNeRF [14] adds camera distortion parameterization and employs geometric loss for ray regularization. Similarly, GARF [14] demonstrates that Gaussian-MLPs facilitate more straightforward and accurate joint optimization of pose and scene. SPARF [31] adds Gaussian noise to simulate noisy camera poses. Recent works, such as Nope-NeRF [5], Lu-NeRF [7], LocalRF [21] and CF-3DGS [10], leverage depth information to constrain NeRF or 3DGS optimization. Very recent work [15] utilizes monocular depth estimator and additional image matching network try to reduce the view number, with roughly hours of optimization for a single scene. These pose-free works generally presume the input are dense video sequences [5, 10] with known viewing order and camera intrinsics [5, 10, 15], and the optimization

for each scene (usually several hours) [5, 10, 15] is even longer than COLMAP with NeRF or 3D-GS variants.

### 3. Method

**Overview** First, we discuss our overall pipeline that integrates Multi-View Stereo (MVS) with 3D-GS to address sparse-view reconstruction in the reliance on SfM and training efficiency (Sec.3.1). Then, we present a efficient, confidence-aware point downsample address scene overparameterization (Sec.3.2). We also present a gradient-based joint optimization framework that relies on photometric loss to align the Gaussians and camera parameters in a self-supervised manner (Sec.3.3). An overview of InstantSplat is provided in Fig.2.

#### 3.1. Stitching MVS with Gaussian Splatting

3D Gaussian Splatting (3D-GS) [16] is an explicit 3D scene representation utilizing a set of 3D Gaussians to model the scene. A 3D Gaussian is parameterized by a mean vector  $\mathbf{x} \in \mathbb{R}^3$  and a covariance matrix  $\Sigma \in \mathbb{R}^{3 \times 3}$ :

$$G(\mathbf{p}) = \frac{1}{(2\pi)^{3/2} |\Sigma|^{1/2}} e^{-\frac{1}{2}(\mathbf{p}-\mathbf{x})^T \Sigma^{-1} (\mathbf{p}-\mathbf{x})} \quad (1)$$

To represent the view-direction-dependent, spherical harmonic (SH) coefficients are attached to each Gaussian, and the color is computed via  $\mathbf{c}(\mathbf{d}) = \sum_{i=1}^n c_i \mathcal{B}_i(\mathbf{d})$ , where  $\mathcal{B}_i$  is the  $i^{\text{th}}$  SH basis. And the color is rendered via  $\mathbf{c} = \sum_{i=1}^n c_i \alpha_i \prod_{j=1}^{i-1} (1 - \alpha_j)$ , where  $c_i$  is the color computed from the SH coefficients of the  $i^{\text{th}}$  Gaussian.  $\alpha_i$  is given by evaluating a 2D Gaussian with covariance multiplied by a learned per-Gaussian opacity. The 2D covariance matrix is calculated by projecting the 3D covariance to the camera coordinate system. The 3D covariance matrix is decomposed into a scaling matrix and a rotation matrix. In summary, 3D-GS uses a set of 3D Gaussians  $\{\mathbf{G}_i | i = 1, 2, \dots, n\}$  to represent a scene, where each 3D Gaussian  $\mathbf{G}_i$  is characterized by: position  $\mathbf{x} \in \mathbb{R}^3$ , a series of SH coefficients  $\{c_i \in \mathbb{R}^3 | i = 1, 2, \dots, n\}$ , opacity  $\alpha \in \mathbb{R}$ , rotation  $\mathbf{q} \in \mathbb{H}$  and scaling  $\mathbf{s} \in \mathbb{R}^3$ .

Although efficient in rendering, the point-based 3D-GS faces an **optimization problem originated from randomly initialized Gaussians or sparse SfM points from COLMAP**. SfM typically fails when matched features are scarce, particularly with sparse-view data. Furthermore, the sequential processing pipeline from COLMAP to GS optimization lacks an error correction mechanism to address accumulated errors, necessitating careful selection of hyperparameters in GS. For example, Adaptive Density Control (ADC) [16] requires a complex strategy to determine when, where, and how to generate new Gaussians, and we show an example in Tab. 1.

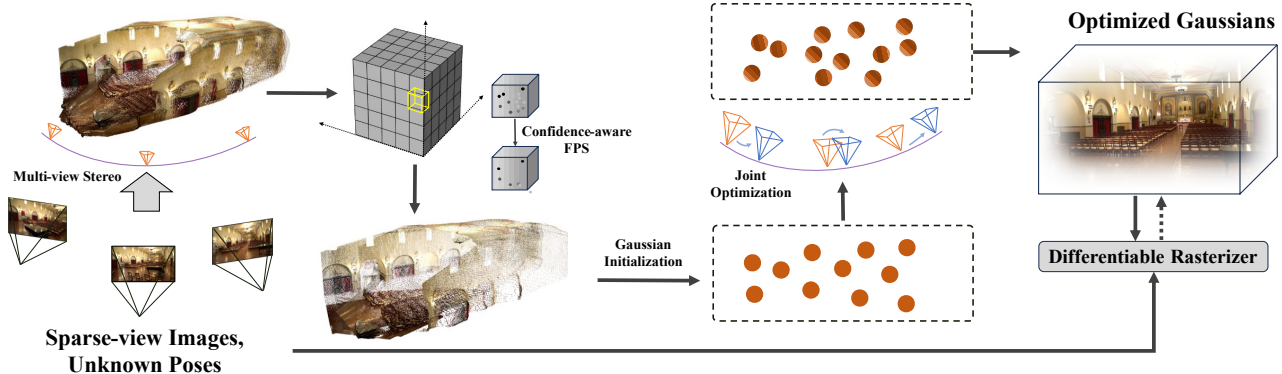


Figure 2. **Overall Framework of InstantSplat.** Beginning with sparse, unposed images, we generate a pixel-wise multi-view dense point cloud utilizing an off-the-shelf model along with computed initial camera poses. We conduct Adaptive Dense Surface Initialization employing a voxel-wise, confidence-aware point downsample to minimize redundancy and achieve uniform sampling. A streamlined Joint Optimization process without ADC is then implemented to adjust the Gaussian and camera parameters, ensuring consistency across multi-view images. All these processes are executed in a matter of seconds.

A straightforward solution is to seek to the dense stereo point cloud which mitigates the issue associated with sensitivity of ADC. However, traditional stereo matching pipeline is inefficient and requires significantly more time than the SfM process. Fortunately, the development of deep learning-based dense stereo frameworks [11, 41] has sped up the inference for predicting scale-related depth maps to milliseconds, though they still assume known camera parameters. Most recently, DUS3R [33] accepts only two images as input and directly generates per-pixel point maps and confidence maps as outputs. A very efficient post-processing optimization can then be leveraged to solve the per-view pixel-to-3D mapping and the incremental relative poses. Specifically, the training objective of DUS3R is based on regression of the unprojected and normalized point maps of two input views. Here, the ground-truth pointmaps from the datasets are  $\hat{\mathbf{P}}_{1,1}$  and  $\hat{\mathbf{P}}_{2,1}$ , obtained from two corresponding views  $\{1, 2\}$  where the camera origin as view 1, on which the ground-truth is defined. The regression loss for training DUS3R is as:

$$\mathcal{L}_{reg} = \left\| \frac{1}{z_i} \cdot \mathbf{P}_{v,1} - \frac{1}{\hat{z}_i} \cdot \hat{\mathbf{P}}_{v,1} \right\| \quad (2)$$

The view  $v \in \{1, 2\}$ ,  $\mathbf{P}$  and  $\hat{\mathbf{P}}$  are the prediction and ground-truth, separately. To handle the scale ambiguity between prediction and ground-truth, DUS3R normalizes the predicted and ground-truth pointmaps by scaling factors  $z_i = \text{norm}(\mathbf{P}_{1,1}, \mathbf{P}_{2,1})$  and  $\hat{z}_i = \text{norm}(\hat{\mathbf{P}}_{1,1}, \hat{\mathbf{P}}_{2,1})$ , respectively, which simply represent the average distance, denoted as  $\mathbf{D}$  of all valid points to the origin. Then, the pixel-wise confidence  $\mathbf{C}_{v,1}^i$  is defined and optimized as:

$$\mathcal{L}_{conf} = \sum_{v \in \{1, 2\}} \sum_{i \in \mathbf{D}^v} \mathbf{C}_{v,1}^i \cdot \mathcal{L}_{reg}(v, i) - \alpha \cdot \log \mathbf{C}_{v,1}^i, \quad (3)$$

where  $\alpha$  is a hyper-parameter controlling the regularization

term, encouraging the network to extrapolate in harder areas.

**Recovering Camera Parameters.** We obtain 1:1 mapping from the pixel lattice to pointmap where we can build the mapping from 2D to the camera coordinate system. We can first solve the simple optimization problem based on the Weiszfeld algorithm [26] to calculate per-camera focal:

$$f^* = \arg \min_f \sum_{i=0}^W \sum_{j=0}^H \mathbf{O}^{i,j} \left\| (i', j') - f \frac{(\mathbf{P}^{i,j,0}, \mathbf{P}^{i,j,1})}{\mathbf{P}^{i,j,2}} \right\| \quad (4)$$

where  $i' = i - \frac{W}{2}$  and  $j' = j - \frac{H}{2}$  denote centered pixel indices. Assuming a single-camera setup similar to that used in COLMAP for a single scene capture, we propose stabilizing the estimated focal length by averaging across all training views:  $\bar{f} = \frac{1}{N} \sum_{i=1}^N f_i^*$ . The resulting  $\bar{f}$  represents the computed focal length that is utilized in subsequent processes. Relative transformation  $\mathbf{T} = [\mathbf{R} | \mathbf{t}]$  can be computed by RANSAC [9] with PnP [12, 18] for each image pair.

**Pair-wise to Globally Aligned Poses.** DUS3R originally takes image pairs as inputs where post-processing is required to align the scale if more than two views are captured from the scene. The underlying reason is that the predicted point map are at the normalized scales within its own, and such misalignment of each independent calculated relative poses leads to significant scale variance, resulting in inaccurate camera poses. Similar to DUS3R we first construct a complete connectivity graph  $\mathcal{G}(\mathcal{V}, \mathcal{E})$  of all the  $N$  input views, where the vertices  $\mathcal{V}$  and each edge  $e = (n, m) \in \mathcal{E}$  indicate a shared visual content between images  $I_n$  and  $I_m$ . To convert the initially predicted point map  $\{(\mathbf{P}_i \in \mathbb{R}^{H \times W \times 3})\}_{i=1}^N$  to be a globally aligned one  $\{(\hat{\mathbf{P}}_i \in \mathbb{R}^{H \times W \times 3})\}_{i=1}^N$ , we update the point maps, transformation matrix, and a scale factor: For the



Figure 3. **Visualizations Before and After Vanilla Downsampling.** Directly downsampling based on the predicted confidence map  $C_i$  results in missing blocks, even when partitioning the scene into  $32^3$  grids. This outcome motivates the development of a more adaptive sampling strategy.

complete graph, any image pair  $e = (n, m) \in \mathcal{E}$ , the point maps  $\mathbf{P}_{n,n}, \mathbf{P}_{m,n}$  and confidence maps  $\mathbf{O}_{n,n}, \mathbf{O}_{m,n}$ . For clarity, let us define  $\mathbf{P}_{n,e} := \mathbf{P}_{n,n}$ , and  $\mathbf{P}_{m,e} := \mathbf{P}_{m,n}$ ,  $\mathbf{O}_{n,e} := \mathbf{O}_{n,n}$ , and  $\mathbf{O}_{m,e} := \mathbf{O}_{m,n}$ . The optimization for the transformation matrix of edge  $\mathbf{T}_e$ , scaling factor  $\sigma_e$  and point map  $\tilde{\mathbf{P}}$  are given by:

$$\tilde{\mathbf{P}}^* = \arg \min_{\tilde{\mathbf{P}}, \mathbf{T}, \sigma} \sum_{e \in \mathcal{E}} \sum_{v \in e} \sum_{i=1}^{HW} \mathbf{O}_{v,e}^i \left\| \tilde{\mathbf{P}}_v^i - \sigma_e \mathbf{T}_e \mathbf{P}_{v,e}^i \right\|. \quad (5)$$

Here, we slightly abuse notation and use  $v \in e$  for  $v \in \{n, m\}$  if  $e = (n, m)$ . The idea is that, for a given pair  $e$ , the same rigid transformation  $\mathbf{T}_e$  should align both pointmaps  $\mathbf{P}_{n,e}$  and  $\mathbf{P}_{m,e}$  with the world-coordinate pointmaps  $\tilde{\mathbf{P}}_{n,e}$  and  $\tilde{\mathbf{P}}_{m,e}$ , since  $\mathbf{P}_{n,e}$  and  $\mathbf{P}_{m,e}$  are by definition both expressed in the same coordinate frame. To avoid the trivial optimum where  $\sigma_e = 0, \forall e \in \mathcal{E}$ , DUS3R enforces  $\prod_e \sigma_e = 1$ . This post-processing step yields a globally aligned point cloud within only seconds, where inferring per-view point and confidence maps can be achieved real-time on a modern GPU.

Having aligned the point clouds, we commence the integration process by initializing 3D Gaussians [16], treating each point as a primitive. However, the dense stereo point cloud is highly overparameterized due to pixel-wise predictions, accompanied by suboptimal pose estimations. As illustrated in the first row of Tab. 4, we observe that the camera poses initialized from pixel-wise point maps differ significantly from those produced by COLMAP when processing all dense sequences. This indicates that naïve integration yields suboptimal results.

### 3.2. Adaptive Dense Surface Point Initialization

We aim to reduce point redundancy starting from the pixel-wise predictions. Specifically, we propose leveraging the initial scene scale and confidence map  $C_{v,1}$  in previous step to perform adaptive point cloud downsampling. This approach is intended to achieve accurate, uniform, and concise initialization. However, simply global or grid-wise confidence-based downsampling induces missing scene blocks (Fig. 3), motivate us to design more adaptive way.

**Adaptive Voxel Grid Partitioning** Given  $N$  points, we dynamically partition the space into  $K = k \times k \times k$  adaptive grids. Each grid, or voxel  $V_j$ , is defined segment boundaries where the entire scene range of each dimension ( $D$ ) is divided into  $k$  equal segments, resulting in adaptive grid boundaries. Each point  $\mathbf{p}_i = (x_i, y_i, z_i)$  is assigned to a voxel based on its coordinate falling within the voxel boundaries:

$$\text{Bound}_D = \left\{ D_{\min} + \frac{n}{k} \cdot (D_{\max} - D_{\min}) \mid n = 0, 1, \dots, k-1 \right\}$$

$$V_j = \{ \mathbf{p}_i \mid \{x_i, y_i, z_i\} \in \{\text{Bound}_x, \text{Bound}_y, \text{Bound}_z\} \}$$

**Confidence-aware Point Cloud Downampling** Within each voxel  $V_j$ , a set of points  $\mathbf{p}_i$  is downsampled. We propose an efficient point downsampler to ensure uniformity while preserving the high-quality surface points. Instead of leveraging the confidence score or employing farthest point sampling (FPS) globally, we utilize FPS within each voxel and perform the computation in parallel. This method selects the point that is farthest from any point already chosen in the sampling process, thereby ensuring spatial diversity. Rather than solely relying on point confidence to select subsets from point clouds, it is observed that raw point clouds exhibit biases towards regions with increased overlap in training images. This bias results in an uneven distribution, where confidence-based sampling alone may lead to the presence of empty regions, as demonstrated in Fig 3.

$$P \leftarrow \{v_i\}, \quad v_i \in V_j \text{ chosen randomly}$$

$$K \leftarrow \left\lfloor |V_j| \cdot \left( \frac{1}{|V_j|} \sum_{v \in V_j} c_v \right) \right\rfloor$$

For  $k = 1$  to  $K$  do

$$v_j \leftarrow \arg \max_{v \in V_j \setminus P} \left( \min_{p \in P} d(v, p) \right)$$

$$P \leftarrow P \cup \{v_j\}$$

where  $P$  is the final returned point set in the voxel,  $d$  denotes the Euclidean distance, and  $K$  is the point number in the  $V_j$ . This step ensures uniformity and enhances the accuracy of the point cloud within each grid, effectively improving the quality of the data for further processing.

### 3.3. Joint Optimization for Alignment

We initialize Gaussians based on the sampled point cloud, employing a heuristic rule as described in 3D-GS [16]. To mitigate the issues arising from noisy point clouds and inaccurate camera poses, we introduce a self-correction mechanism. This mechanism efficiently adapts parameters through the use of photometric loss, applicable to both camera and Gaussian parameters.

Table 2. **Quantitative Evaluations on Tanks and Temples Datasets.** Our method renders significantly clearer details (as measured by LPIPS) compared to other pose-free methods, even with an optimization period of only  $\sim 10$  seconds (**Ours-S**), and is devoid of artifacts typically associated with noisy pose estimation (as quantified by ATE). Extending the training time can further enhance the rendering quality. To ensure fair comparisons, we executed 3D-GS and FSGS using COLMAP on the same number of views as the other pose-free methods, whereas COLMAP fails when only three views are available. InstantSplat demonstrates better camera pose estimation accuracy in the Absolute Trajectory Error (ATE), as quantified using the ground truth scale. In 3D-GS, ADC stands for Adaptive Density Control [16].

	Requirements	Training Time			SSIM			LPIPS			ATE		
		3-view	6-view	12-view	3-view	6-view	12-view	3-view	6-view	12-view	3-view	6-view	12-view
COLMAP + 3DGS [16]	COLMAP K, Pose	-	6min44s	8min11	-	0.5917	0.7163	-	0.3433	0.2505	-	0.0070	0.0026
COLMAP + FSGS [45]	COLMAP and ADC	-	3min16s	3min49s	-	0.7752	0.8479	-	0.1927	0.1477	-	0.0070	0.0026
NoPe-NeRF [5]	GT K	33min 1min6s	47min 2min14s	84min 3min30s	0.4570 0.4066	0.5067 0.4690	0.6096 0.5077	0.6168 0.4520	0.5780 0.4219	0.5067 0.4189	0.2828 0.1937	0.1431 0.1572	0.1029 0.1031
CF-3DGS [10]													
NeRF-mm [35]	Joint Optimization	7min42s	14min40s	29min42s	0.4019	0.4308	0.4677	0.6421	0.6252	0.6020	0.2721	0.2329	0.1529
<b>Ours-S</b>		10.4s	15.7s	32.5s	<b>0.7425</b>	0.8241	0.8172	0.2190	0.1892	0.2199	0.0153	0.0199	0.0143
<b>Ours-XL</b>	Coarse-to-fine	28.6s	34.1s	61.6s	0.7380	<b>0.8454</b>	<b>0.8795</b>	<b>0.1822</b>	<b>0.1212</b>	<b>0.1093</b>	<b>0.0150</b>	0.0197	0.0143

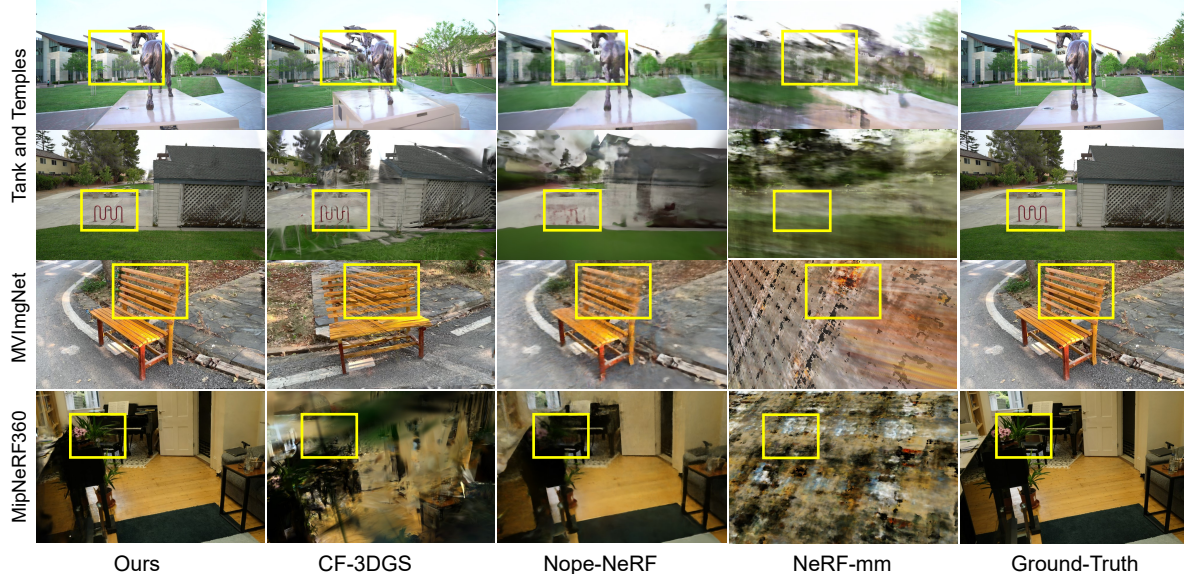


Figure 4. **Visual Comparisons** between InstantSplat and various pose-free baseline methods. InstantSplat achieves faithful 3D reconstruction and renders novel views with as few as three training images on the Tanks and Temples datasets, and the MVImgNet datasets. On the most challenging MipNeRF360 datasets, which feature 360° captured views at different elevations—a scenario not previously explored in pose-free literature—InstantSplat still manages to reconstruct a reasonable scene representation, thus enabling rendering of novel views. We omit comparisons with 3D-GS and FSGS as they require COLMAP for obtaining SfM poses, and COLMAP fails in these settings.

**Gradient-Based Optimization under Self-Supervision**  
Given multiple views and a coarse 3D model characterized by noisy poses, represented by a set of Gaussians  $\mathbf{G}$ , and  $\mathbf{T}$ , we explore the application of gradient descent to minimize the residual between GT pixels and rendered from the model. Specifically, we conduct joint optimization of all Gaussian parameters and adjust the camera parameters. This adjustment allows  $\mathbf{G}$  to achieve reduced photometric errors at a target view position  $\mathbf{T}$ . The formulation is as follows:

$$\mathbf{G}^*, \mathbf{T}^* = \arg \min_{\mathbf{G}, \mathbf{T}} \sum_{v \in N} \sum_{i=1}^{HW} \left\| \tilde{C}_v^i(\mathbf{G}, \mathbf{T}) - C_v^i(\mathbf{G}, \mathbf{T}) \right\| \quad (6)$$

**Aligning Camera Poses on Test Views** In contrast to the conventional approach where exact camera poses for test

views are known and typically estimated alongside training views within the same coordinate system (as seen in 3D-GS [16] and NeRF [23]), our scenario involves test views with either unknown or noisy poses. Similar to NeRF-based works [35], we maintain the GS model trained on training views, in a frozen state while optimizing the camera poses for test views. This optimization process focuses on minimizing the photometric discrepancies (Eq. 6) between the synthesized images and the actual test views, aiming to achieve a more precise alignment for evaluation. This step is performed for 500 iterations per-image.

Table 3. **Quantitative Evaluations on MVImgNet and MipNeRF360 Datasets.** Our method renders significantly clearer details (by LPIPS) compared to other pose-free methods, devoid of artifacts typically associated with noisy pose estimation (e.g., CF-3DGS [10], NeRFmm [35]) and NoPe-NeRF [5]. COLMAP on full views as the ground-truth reference. Our method produces more accurate camera pose estimation in the Absolute Trajectory Error (ATE) than previous COLMAP-free methods, quantified using the ground truth scale. ADC is denoted as Adaptive Density Control [16].

	Requirements	MVImgNet (3 Training Views)					MipNeRF360 (12 Training Views)				
		Time	SSIM	PSNR	LPIPS	ATE $\downarrow$	Time	SSIM	PSNR	LPIPS	ATE $\downarrow$
NoPe-NeRF	GT K	37min42s	0.4326	15.34	0.6674	0.2780	78min31s	0.3580	16.16	0.6867	0.2374
		3min47s	0.3414	13.40	0.5523	0.1593	5min58s	0.2443	13.17	0.6098	0.2263
NeRF-mm	Joint Optimization	8min35s	0.3752	13.04	0.7001	0.2376	28min10s	0.2003	11.53	0.7238	0.2401
<b>Our-S</b>	Coarse-to-fine	13.5s	<b>0.5569</b>	17.71	0.3806	<b>0.0282</b>	45.3s	<b>0.4647</b>	<b>17.68</b>	0.5027	<b>0.2161</b>
<b>Our-XL</b>		37.5s	0.5451	<b>17.54</b>	<b>0.3526</b>	0.0283	1min19s	0.4398	17.23	<b>0.4486</b>	0.2162

## 4. Experiments

### 4.1. Experimental Setup

**Datasets.** Experiments follow previous pose-free methods [5, 10], we utilized all eight scenes from the **Tanks and Temples** datasets [17] with various view numbers. We also extracted seven outdoor scenes from the **MVImgNet** datasets [43], which includes diverse scene types such as Car, Suv, Bicycle, Chair, Ladder, Bench, and Table. We perform the first attempt of on **MipNeRF360** [2] datasets and evaluate with pose-free methods, using 12 training views. We also test InstantSplat on in-the-wild data, including the **Sora** video, by extracting the first, middle, and last frames, use navigation stereo camera data from the **Perseverance Rover** available on the **NASA website**, and leverage randomly sampled three training views from DL3DV-10K datasets [20]. We will release the code and data.

**Train/Test Datasets Split.** We sample 24 images from the datasets for both training and evaluation, covering the entire set. Test images (12, excluding the first and last images) are uniformly chosen for all settings, and  $N$  training images are uniformly selected from the remaining 12 images for sparse-view training. Specifically, 24 images are uniformly sampled from both MVImgNet and Tank and Temples, while for MipNeRF360, the selection is made from the first 48 frames as it is captured from different elevations over a full 360-degree rotation. We vary the sparse-view number  $N$  from 3 to 12 to evaluate all adopted algorithms.

**Metrics.** We evaluate two tasks on benchmark datasets [17, 43]: novel view synthesis and camera pose estimation. For novel view synthesis, we use standard evaluation metrics, including Peak Signal-to-Noise Ratio (PSNR), Structural Similarity Index Measure (SSIM) [34], and Learned Perceptual Image Patch Similarity (LPIPS) [44]. We report the errors in camera rotation and translation, focusing on Absolute Trajectory Error (ATE) and Relative Pose Error (RPE), as specified in [5]. COLMAP

Table 4. **Ablation Study** for validating design choices. We opt for the **XL** setting, where 1,000 iterations are adopted to ensure reconstruction quality.

Model	Train $\downarrow$	FPS $\uparrow$	SSIM $\uparrow$	LPIPS $\downarrow$	RPE $\downarrow$	RPE $\downarrow$	ATE $\downarrow$
Baseline by Stitching	55.6s	150	0.6317	0.2445	2.7651	0.2540	0.0276
+Focal Averaging(Sec. 3.1)	55.6s	150	0.7564	0.2012	2.7896	0.2480	0.0297
+Adaptive Dense Surface Init(Sec. 3.2)	54.4s	204	0.7599	0.1977	2.7896	0.2480	0.0297
+Joint Optimization(Sec. 3.3)	<b>54.4s</b>	<b>204</b>	<b>0.8044</b>	<b>0.1688</b>	<b>2.5544</b>	<b>0.2052</b>	0.0284
Adaptive Dense Surface Init(Sec. 3.2)							
Global + Confidence?	52.9s	204	0.7202	0.2599	2.5691	0.2039	0.0285
Global + FPS?	>10min	204	0.8006	0.1717	2.5469	0.2036	0.0285
Grid-based FPS (6 $^3$ )	57.0s	204	0.8026	0.1690	2.5418	0.2040	0.0284
Grid-based FPS + Confidence (4 $^3$ )	293.9s	164	0.8033	0.1690	2.5347	0.2053	0.0284
Grid-based FPS + Confidence (8 $^3$ )	96.8s	181	0.7978	0.1731	2.5445	0.2062	0.0284
Grid-based FPS + Confidence (16 $^3$ )	53.5s	198	0.8006	0.1732	2.5561	0.2056	0.0285
Grid-based FPS + Confidence (32 $^3$ )	51.8s	200	0.8031	0.1691	2.5398	0.2032	0.0284
Grid-based FPS + Confidence (64 $^3$ )	54.4s	<b>204</b>	<b>0.8044</b>	<b>0.1688</b>	<b>2.5544</b>	0.2053	<b>0.0284</b>
InstantSplat	54.4s	204	0.8044	0.1688	2.5544	0.2053	0.0284

poses from all dense views are employed as ground-truth references.

**Baselines.** Our comparisons on pose-free methods include Nope-NeRF [5] and CF-3DGS [10], both supported by monocular depth maps and ground-truth camera intrinsics. We also consider NeRFmm [35], which involves joint optimization of NeRF and all camera parameters. Additionally, we compare our method with 3D-GS [16] and FSGS [45], which utilize COLMAP for pre-computing the camera parameters.

**Implementation Details.** Our implementation leverages the PyTorch framework, The optimization iterations is set 200 for **Ours-S**, and 1,000 for **Ours-XL**, achieving balanced quality and training efficiency. DUST3R [33] a resolution of 512 are used for predicting MVS depth maps. We perform experiments on one Nvidia A100 GPU for fair comparisons.

### 4.2. Experimental Results

**Quantitative and Qualitative Results** Evaluations of tasks such as novel view synthesis and pose estimation on the Tanks and Temples datasets are summarized in Tab.2 and Fig.4. Nope-NeRF [5], which utilizes Multilayer Perceptrons (MLPs), achieves promising results in rendering quality and pose estimation accuracy. However, it tends to produce overly blurred images (see the third column in

Fig.4), attributed to the intensive constraints imposed by its geometric field, and exhibits long training for a single scene and inference times ( $\sim 3$  seconds per frame) for rendering one image. CF-3DGS[10], which employs Gaussian Splatting and integrates both local and global optimization stages with adaptive density control and opacity reset policies, is prone to artifacts when rendering on new viewpoints, a result of the intricate optimization process coupled with erroneous pose estimations, as depicted in Fig. 4. Moreover, both Nope-NeRF and CF-3DGS assume known and accurate focal lengths. NeRFmm, which aims to concurrently optimize camera parameters and the radiance field, tends to yield suboptimal results due to the inherent challenges of naive joint optimization. The pose metrics reveal artifacts attributable to sparse observations and inaccurately estimated poses, shown in Tab. 2. This issue is particularly detrimental for CF-3DGS and Nope-NeRF, which rely on dense video sequences similar to SLAM, thereby struggling in when sampling dense video frames into sparse multi-view images. Conversely, our method, which initializes with MVS scene structure and employs a gradient-based joint optimization process, offers enhanced robustness and superior performance. Additional experiments on the MVImgnet datasets using three training images, and on the MipNeRF360 datasets with 12 training views are demonstrated in Tab. 3. It worth to note that, InstantSplat consistently outperforms all baselines across all evaluated datasets and visual metrics. Please refer to our supplementary video for more visualization, with in-the-wild test case include Sora video and stereo image pairs from Mars rover.

### 4.3. Ablations and Analysis

We conducted ablation studies to validate our design choices, transitioning from the use of non-differentiable Structure-from-Motion (SfM) complemented by Gaussian Splatting with adaptive density control, to adopting Multi-View Stereo (MVS) with Adaptive Surface Point Down-sampling and Joint Optimization for efficient and robust sparse-view 3D modeling. Experiments were conducted using 12 training views on the Church scene, with COLMAP poses derived from 400 dense views serving as ground truth, unless otherwise specified.

- Question 1: What is the quality of the multi-view stereo predictions?
- Question 2: What is the effect of focal averaging?
- Question 3: Is adaptive dense surface initialization effective in reducing redundancy while preserving reconstruction accuracy?
- Question 4: Is joint optimization necessary to achieve accurate rendering?
- Question 5: Can InstantSplat, using sparse-view images, match the rendering quality of previous methods that utilized dense-view configurations?

Table 5. Performance comparison between InstantSplat (ours) with 24 training views, CF-3DGS and 3D-GS with dense (100-400) training views on the Tanks and Temples dataset. We report the LPIPS, reconstruction time, and pose accuracy.

	Views $\downarrow$	Time $\downarrow$	LPIPS $\downarrow$	ATE $\downarrow$
CF-3DGS [10]	100-400	$\sim 30$ min	0.09	0.004
COLMAP+3DGS [16]	100-400	$\sim 30$ min	0.10	-
InstantSplat (Ours)	12	$\sim 1$ min	0.10	0.014

We assess the accuracy of camera poses derived from the MVS point map as detailed in Section 3.1. As illustrated in the first and fourth rows of Tab. 4, there exists considerable scope for enhancing the MVS-initialized scene geometry.

Aggregating the focal lengths from all images provides a stable basis for optimizing the 3D representation, as shown in the second row, and the view synthesis quality is significantly boosted.

The adaptive dense surface initialization, utilizing parallel grid-based Farthest Point Sampling (FPS) that accounts for confidence levels, enables effective down-sampling which reduces redundancy while preserving accuracy (refer to the third row). We choose  $64^3$  grids in our experiments.

Joint optimization, employing a coarse 3D model and photometric errors, can further enhance both rendering and pose accuracy.

The evaluation of InstantSplat with 12 training images demonstrates close proximity in rendering quality using the Learned Perceptual Image Patch Similarity (LPIPS), nearly akin to human perception. Nonetheless, there remains a discrepancy in pose estimation accuracy as measured by the Absolute Trajectory Error (ATE).

## 5. Conclusion

We introduced InstantSplat, a framework designed to reconstruct scenes from sparse-view, unposed images within seconds. Our approach utilizes the capabilities of multi-view stereo (MVS) for coarse scene initialization and proposes a gradient-based joint optimization for Gaussian attributes and camera parameters in a self-supervised manner. Compared with previous best-performing pose-free methods [5, 10], we have reduced the requisite number of views from hundreds [5, 10] to just a few, thereby enabling large-scale 3D modeling with only a minimal number of images and unposed views.

However, InstantSplat is constrained by the requirement of MVS for a globally aligned point cloud in scenes with more than hundreds of images. Addressing this limitation through progressive alignment will be explored in future works.

## References

[1] Shai Avidan and Amnon Shashua. Novel view synthesis in tensor space. In *Proceedings of IEEE Computer Society Conference on Computer Vision and Pattern Recognition*, pages 1034–1040. IEEE, 1997. 2

[2] Jonathan T. Barron, Ben Mildenhall, Dor Verbin, Pratul P. Srinivasan, and Peter Hedman. Mip-NeRF 360: Unbounded Anti-Aliased Neural Radiance Fields. *2022 IEEE/CVF Conference on Computer Vision and Pattern Recognition (CVPR)*, pages 5460–5469, 2022. 2, 7

[3] Jonathan T Barron, Ben Mildenhall, Dor Verbin, Pratul P Srinivasan, and Peter Hedman. Mip-nerf 360: Unbounded anti-aliased neural radiance fields. In *Proceedings of the IEEE/CVF Conference on Computer Vision and Pattern Recognition*, pages 5470–5479, 2022.

[4] Jonathan T Barron, Ben Mildenhall, Dor Verbin, Pratul P Srinivasan, and Peter Hedman. Zip-nerf: Anti-aliased grid-based neural radiance fields. In *Proceedings of the IEEE/CVF International Conference on Computer Vision*, pages 19697–19705, 2023. 2

[5] Wenjing Bian, Zirui Wang, Kejie Li, Jia-Wang Bian, and Victor Adrian Prisacariu. Nope-nerf: Optimising neural radiance field with no pose prior. In *Proceedings of the IEEE/CVF Conference on Computer Vision and Pattern Recognition*, pages 4160–4169, 2023. 2, 3, 6, 7, 8

[6] Zhang Chen, Zhong Li, Liangchen Song, Lele Chen, Jingyi Yu, Junsong Yuan, and Yi Xu. Neurbf: A neural fields representation with adaptive radial basis functions. In *Proceedings of the IEEE/CVF International Conference on Computer Vision*, pages 4182–4194, 2023. 2

[7] Zehzhou Cheng, Carlos Esteves, Varun Jampani, Abhishek Kar, Subhransu Maji, and Ameesh Makadia. Lu-nerf: Scene and pose estimation by synchronizing local unposed nerfs. In *Proceedings of the IEEE/CVF International Conference on Computer Vision*, pages 18312–18321, 2023. 3

[8] Kangle Deng, Andrew Liu, Jun-Yan Zhu, and Deva Ramanan. Depth-supervised nerf: Fewer views and faster training for free. *arXiv preprint arXiv:2107.02791*, 2021. 3

[9] Martin A Fischler and Robert C Bolles. Random sample consensus: a paradigm for model fitting with applications to image analysis and automated cartography. *Communications of the ACM*, 24(6):381–395, 1981. 4

[10] Yang Fu, Sifei Liu, Amey Kulkarni, Jan Kautz, Alexei A Efros, and Xiaolong Wang. Colmap-free 3d gaussian splatting. *arXiv preprint arXiv:2312.07504*, 2023. 2, 3, 6, 7, 8

[11] Xiaodong Gu, Zhiwen Fan, Siyu Zhu, Zuozhuo Dai, Feitong Tan, and Ping Tan. Cascade cost volume for high-resolution multi-view stereo and stereo matching. In *Proceedings of the IEEE/CVF conference on computer vision and pattern recognition*, pages 2495–2504, 2020. 2, 4

[12] Richard Hartley and Andrew Zisserman. *Multiple view geometry in computer vision*. Cambridge university press, 2003. 4

[13] Ajay Jain, Matthew Tancik, and Pieter Abbeel. Putting nerf on a diet: Semantically consistent few-shot view synthesis. In *Proceedings of the IEEE/CVF International Conference on Computer Vision*, pages 5885–5894, 2021. 1, 2, 3

[14] Yoonwoo Jeong, Seokjun Ahn, Christopher Choy, Anima Anandkumar, Minsu Cho, and Jaesik Park. Self-calibrating neural radiance fields. In *Proceedings of the IEEE/CVF International Conference on Computer Vision*, pages 5846–5854, 2021. 3

[15] Kaiwen Jiang, Yang Fu, Yash Belhe, Xiaolong Wang, Hao Su, Ravi Ramamoorthi, et al. A construct-optimize approach to sparse view synthesis without camera pose. *arXiv preprint arXiv:2405.03659*, 2024. 3

[16] Bernhard Kerbl, Georgios Kopanas, Thomas Leimkühler, and George Drettakis. 3d gaussian splatting for real-time radiance field rendering. *ACM Transactions on Graphics (ToG)*, 42(4):1–14, 2023. 2, 3, 5, 6, 7, 8

[17] Arno Knapitsch, Jaesik Park, Qian-Yi Zhou, and Vladlen Koltun. Tanks and temples: Benchmarking large-scale scene reconstruction. *ACM Transactions on Graphics (ToG)*, 36(4):1–13, 2017. 2, 7

[18] Vincent Lepetit, Francesc Moreno-Noguer, and Pascal Fua. Ep np: An accurate o (n) solution to the p np problem. *International journal of computer vision*, 81:155–166, 2009. 4

[19] Chen-Hsuan Lin, Wei-Chiu Ma, Antonio Torralba, and Simon Lucey. Barf: Bundle-adjusting neural radiance fields. In *Proceedings of the IEEE/CVF International Conference on Computer Vision*, pages 5741–5751, 2021. 3

[20] Lu Ling, Yichen Sheng, Zhi Tu, Wentian Zhao, Cheng Xin, Kun Wan, Lantao Yu, Qianyu Guo, Zixun Yu, Yawen Lu, et al. Dl3dv-10k: A large-scale scene dataset for deep learning-based 3d vision. *arXiv preprint arXiv:2312.16256*, 2023. 7

[21] Andreas Meuleman, Yu-Lun Liu, Chen Gao, Jia-Bin Huang, Changil Kim, Min H Kim, and Johannes Kopf. Progressively optimized local radiance fields for robust view synthesis. In *Proceedings of the IEEE/CVF Conference on Computer Vision and Pattern Recognition*, pages 16539–16548, 2023. 3

[22] Ben Mildenhall, Pratul P Srinivasan, Rodrigo Ortiz-Cayon, Nima Khademi Kalantari, Ravi Ramamoorthi, Ren Ng, and Abhishek Kar. Local light field fusion: Practical view synthesis with prescriptive sampling guidelines. *ACM Transactions on Graphics (TOG)*, 38(4):1–14, 2019. 2

[23] Ben Mildenhall, Pratul P Srinivasan, Matthew Tancik, Jonathan T Barron, Ravi Ramamoorthi, and Ren Ng. Nerf: Representing Scenes As Neural Radiance Fields for View Synthesis. *Communications of the ACM*, 65(1):99–106, 2021. 2, 6

[24] Michael Niemeyer, Jonathan T Barron, Ben Mildenhall, Mehdi SM Sajjadi, Andreas Geiger, and Noha Radwan. Reg-nerf: Regularizing neural radiance fields for view synthesis from sparse inputs. *arXiv preprint arXiv:2112.00724*, 2021. 1, 2, 3

[25] Eric Penner and Li Zhang. Soft 3D Reconstruction for View Synthesis. *ACM Transactions on Graphics (TOG)*, 36(6):1–11, 2017. 2

[26] F Plastria. The weiszfeld algorithm: proof, amendments and extensions, ha eiselt and v. marianov (eds.) foundations of location analysis, international series in operations research and management science, 2011. 4

[27] Johannes L Schonberger and Jan-Michael Frahm. Structure-from-motion revisited. In *Proceedings of the IEEE conference on computer vision and pattern recognition*, pages 4104–4113, 2016. 2, 3

[28] Steven M Seitz and Charles R Dyer. Photorealistic Scene Reconstruction by Voxel Coloring, 2002. US Patent 6,363,170. 2

[29] Pratul P Srinivasan, Richard Tucker, Jonathan T Barron, Ravi Ramamoorthi, Ren Ng, and Noah Snavely. Pushing the Boundaries of View Extrapolation With Multiplane Images. In *Proceedings of the IEEE/CVF Conference on Computer Vision and Pattern Recognition*, pages 175–184, 2019.

[30] Pratul P Srinivasan, Ben Mildenhall, Matthew Tancik, Jonathan T Barron, Richard Tucker, and Noah Snavely. Lighthouse: Predicting Lighting Volumes for Spatially-Coherent Illumination. In *Proceedings of the IEEE/CVF Conference on Computer Vision and Pattern Recognition*, pages 8080–8089, 2020. 2

[31] Prune Truong, Marie-Julie Rakotosaona, Fabian Manhardt, and Federico Tombari. Sparf: Neural radiance fields from sparse and noisy poses. In *Proceedings of the IEEE/CVF Conference on Computer Vision and Pattern Recognition*, pages 4190–4200, 2023. 3

[32] Guangcong Wang, Zhaoxi Chen, Chen Change Loy, and Ziwei Liu. Sparsenerf: Distilling depth ranking for few-shot novel view synthesis. *arXiv preprint arXiv:2303.16196*, 2023. 1, 3

[33] Shuzhe Wang, Vincent Leroy, Yohann Cabon, Boris Chidlovskii, and Jerome Revaud. Dust3r: Geometric 3d vision made easy. *arXiv preprint arXiv:2312.14132*, 2023. 2, 4, 7

[34] Zhou Wang, Alan C Bovik, Hamid R Sheikh, and Eero P Simoncelli. Image quality assessment: from error visibility to structural similarity. *IEEE transactions on image processing*, 13(4):600–612, 2004. 7

[35] Zirui Wang, Shangzhe Wu, Weidi Xie, Min Chen, and Victor Adrian Prisacariu. Nerf–: Neural radiance fields without known camera parameters. *arXiv preprint arXiv:2102.07064*, 2021. 2, 3, 6, 7

[36] Rundi Wu, Ben Mildenhall, Philipp Henzler, Keunhong Park, Ruiqi Gao, Daniel Watson, Pratul P Srinivasan, Dor Verbin, Jonathan T Barron, Ben Poole, et al. Reconfusion: 3d reconstruction with diffusion priors. *arXiv preprint arXiv:2312.02981*, 2023. 3

[37] Haolin Xiong, Sairisheek Muttukuru, Rishi Upadhyay, Pradyumna Chari, and Achuta Kadambi. Sparsegs: Real-time 360  $\{\backslash\deg\}$  sparse view synthesis using gaussian splatting. *arXiv preprint arXiv:2312.00206*, 2023. 3

[38] Dejia Xu, Yifan Jiang, Peihao Wang, Zhiwen Fan, Humphrey Shi, and Zhangyang Wang. Sinnerf: Training neural radiance fields on complex scenes from a single image. In *European Conference on Computer Vision*, pages 736–753. Springer, 2022. 3

[39] Qiangeng Xu, Zexiang Xu, Julien Philip, Sai Bi, Zhixin Shu, Kalyan Sunkavalli, and Ulrich Neumann. Pointnerf: Point-based neural radiance fields. In *Proceedings of the IEEE/CVF conference on computer vision and pattern recognition*, pages 5438–5448, 2022. 2

[40] Jiawei Yang, Marco Pavone, and Yue Wang. Freenerf: Improving few-shot neural rendering with free frequency regularization. In *Proceedings of the IEEE/CVF Conference on Computer Vision and Pattern Recognition*, pages 8254–8263, 2023. 1, 3

[41] Yao Yao, Zixin Luo, Shiwei Li, Tian Fang, and Long Quan. Mvsnet: Depth inference for unstructured multi-view stereo. In *Proceedings of the European conference on computer vision (ECCV)*, pages 767–783, 2018. 2, 4

[42] Alex Yu, Vickie Ye, Matthew Tancik, and Angjoo Kanazawa. pixelnerf: Neural radiance fields from one or few images. In *Proceedings of the IEEE/CVF Conference on Computer Vision and Pattern Recognition*, pages 4578–4587, 2021. 3

[43] Xianggang Yu, Mutian Xu, Yidan Zhang, Haolin Liu, Chongjie Ye, Yushuang Wu, Zizheng Yan, Chenming Zhu, Zhangyang Xiong, Tianyou Liang, et al. Mvimgnet: A large-scale dataset of multi-view images. In *Proceedings of the IEEE/CVF conference on computer vision and pattern recognition*, pages 9150–9161, 2023. 2, 7

[44] Richard Zhang, Phillip Isola, Alexei A Efros, Eli Shechtman, and Oliver Wang. The unreasonable effectiveness of deep features as a perceptual metric. In *Proceedings of the IEEE conference on computer vision and pattern recognition*, pages 586–595, 2018. 7

[45] Zehao Zhu, Zhiwen Fan, Yifan Jiang, and Zhangyang Wang. Fsgs: Real-time few-shot view synthesis using gaussian splatting. *arXiv preprint arXiv:2312.00451*, 2023. 3, 6, 7

[46] Matthias Zwicker, Hanspeter Pfister, Jeroen Van Baar, and Markus Gross. Ewa volume splatting. In *Proceedings Visualization, 2001. VIS'01.*, pages 29–538. IEEE, 2001. 2